

NUMERICAL SOLUTIONS FOR THE ORBITAL MOTION OF THE SOLAR SYSTEM OVER THE PAST 100 MYR: LIMITS AND NEW RESULTS ^{*}

RICHARD E. ZEEBE¹

¹SOEST, University of Hawaii at Manoa, 1000 Pope Road, MSB 629, Honolulu, HI 96822, USA. email: zeebe@soest.hawaii.edu

The Astronomical Journal, 154:193, 2017

October 29, 2017

^{*} Numerical solutions are freely available at: www2.hawaii.edu/~zeebe/Astro.html

ABSTRACT

I report results from accurate numerical integrations of Solar System orbits over the past 100 Myr with the integrator package *HNBody*. The simulations used different integrator algorithms, step sizes, initial conditions, and included effects from general relativity, different models of the Moon, the Sun's quadrupole moment, and up to sixteen asteroids. I also probed the potential effect of a hypothetical Planet 9, using one set of possible orbital elements. The most expensive integration (Bulirsch-Stoer) required 4 months wall-clock time with a maximum relative energy error $\lesssim 3 \times 10^{-13}$. The difference in Earth's eccentricity ($\Delta e_{\mathcal{E}}$) was used to track the difference between two solutions, considered to diverge at time τ when $\max|\Delta e_{\mathcal{E}}|$ irreversibly crossed $\sim 10\%$ of mean $e_{\mathcal{E}}$ ($\sim 0.028 \times 0.1$). The results indicate that finding a unique orbital solution is limited by initial conditions from current ephemerides and asteroid perturbations to ~ 54 Myr. Bizarrely, the 4-month Bulirsch-Stoer integration and a symplectic integration that required only 5 hours wall-clock time (12-day time step, Moon as a simple quadrupole perturbation), agree to ~ 63 Myr. Internally, such symplectic integrations are remarkably consistent even for large time steps, suggesting that the relationship between time step and τ is not a robust indicator for the absolute accuracy of symplectic integrations. The effect of a hypothetical Planet 9 on $\Delta e_{\mathcal{E}}$ becomes discernible at ~ 65 Myr. Using τ as a criterion, the current state-of-the-art solutions all differ from previously published results beyond ~ 50 Myr. I also conducted an eigenmode analysis, which provides some insight into the chaotic nature of the inner Solar System. The current study provides new orbital solutions for applications in geological studies.

Keywords: celestial mechanics — methods: numerical — planets and satellites: dynamical evolution and stability

1. INTRODUCTION

The dynamical properties of the Solar System are of continuing interest to a number of fundamental, as well as applied research areas in a variety of scientific disciplines. For example, several studies have recently revisited the Solar System's dynamic stability on billion-year time scale using long-term numerical integrations (e.g., [Batygin & Laughlin 2008](#); [Laskar & Gastineau 2009](#); [Zeebe 2015a,b](#)). Another area of active research concerns the application of astronomical solutions for Earth's orbital parameters in the geological sciences, with vital importance for astrochronology, cyclostratigraphy, and paleoclimatology (e.g., [Laskar et al. 2011a](#); [Westerhold et al. 2012](#); [Ma et al. 2017](#); [Zeebe et al. 2017](#)). Orbital solutions in geological applications are most heavily used over the past ~ 100 Myr, which is the fo-

cus of the present study. In particular, extending an astronomically-tuned geologic time scale further back in time would represent a major advance in that field. Currently, the limit to identifying a unique orbital solution is ~ 50 Myr BP, as small differences in initial conditions or other parameters cause astronomical solutions to diverge around that time, due to the chaotic nature of the system. Hence one focus of the present study will be to determine the divergence time between two solutions (defined below). In addition to far-reaching goals such as improvement of the geologic time scale, orbital solutions are key to a variety of specific applications, including resolving the precise timing of early Paleogene climate events of extreme warmth (so-called hyperthermals), relative to orbital forcing (e.g., [Zachos et al. 2008](#)).

It appears that the numerical solutions for Earth's eccentricity that have hitherto been used in paleoclimate

studies were provided by only two different groups that integrated the full Solar System equations over the past few 100 Myr (e.g., [Varadi et al. 2003](#); [Laskar et al. 2004](#); [Laskar et al. 2011a](#)). Given one numerical realization of a Solar System model (i.e., via one code or integrator package), various parameters determine the properties of the astronomical solution and usually limit its validity to a certain time period. Such limitations may be considered internal and include limitations due to the underlying physics/physical model and numerics. The physics include, for instance, initial coordinates and velocities of Solar System bodies, treatment of the Moon and asteroids, effects from general relativity, the Sun’s quadrupole moment, and the intrinsic dynamics of the system, e.g., its chaotic nature. Numerical issues include, for instance, the type of solver algorithm, numerical accuracy (e.g., time step), round-off errors, and choice of integrator coordinates ([Zeebe 2015a](#)). At present, internal limitations seem to restrict the validity of astronomical solutions to perhaps the past 50 Myr ([Laskar et al. 2011a,b](#)). However, little is currently known about external limitations, that is, how different numerical realizations compare, say, between different investigator groups using different codes and integrator packages. Also, a one-to-one comparison of orbital solutions obtained with fundamentally different algorithms such as Bulirsch-Stoer (BS) and symplectic integrators (yet otherwise identical setup) appears to be missing (‘symplectic integrators’ here refers to N -body maps, e.g., [Wisdom & Holman 1991](#)).

In this paper, I present new results from state-of-the-art Solar System integrations over the past 100 Myr to address the outstanding questions posed above. I provide several new astronomical solutions for Earth’s eccentricity for applications in geological studies.¹ I also investigated the effect of a hypothetical Planet 9, though only for a single set of orbital elements as proposed in the literature. Furthermore, I performed an eigenmode analysis to gain some insight into the chaotic behavior of the system. Finally, I discuss the main factors that currently limit identification of a unique orbital solution beyond ~ 50 Myr.

2. METHODS

The integrations were performed with the integrator package *HNBODY* ([Rauch & Hamilton 2002](#)) using the Bulirsch-Stoer integrator with relative accuracy ϵ_{BS} and the symplectic integrator ([Wisdom & Holman 1991](#)) with time step Δt (Table 1). Relativistic corrections ([Einstein 1916](#)) are critical ([Varadi et al. 2003](#); [Laskar et al. 2004](#); [Zeebe 2015a](#)) and are available in *HNBODY* as Post-Newtonian effects due to the dominant mass.

¹ Numerical solutions are freely available at: www2.hawaii.edu/~zeebe/Astro.html

Hence all simulations presented here include contributions from general relativity (GR). Also, all symplectic integrations were carried out using Jacobi coordinates ([Wisdom & Holman 1991](#)), rather than heliocentric coordinates ([Zeebe 2015a](#)). In this study, wall-clock times refer to *HNBODY-v1.0.10*, double precision on 64-bit Linux machines with Intel i7-3770 3.40 GHz cores.

2.1. Treatment of the Moon

The Moon was included as a separate object (BS and symplectic option *ems*), or the Earth-Moon system was modeled as a gravitational quadrupole (symplectic option *1un*, see Table 1) ([Quinn et al. 1991](#); [Varadi et al. 2003](#); [Rauch & Hamilton 2002](#)). The *ems* option includes a symplectic, self-consistent sub-integration of the Earth-Moon-Sun system; the remaining Solar System bodies treat the Earth-Moon barycenter as a single object ([Rauch & Hamilton 2002](#)). The *1un* option considers the Moon’s influence on the net motion of the Earth-Moon barycenter via a mean quadrupole potential with a correction factor $f_{1un} = 0.8525$ ([Quinn et al. 1991](#); [Varadi et al. 2003](#); [Rauch & Hamilton 2002](#)). The effect of tidal dissipation in the Earth-Moon system was tested in the solution ZB17k following [Quinn et al. \(1991\)](#), using a constant secular change in semimajor axis close to the modern value of $\dot{a} \simeq 3.8 \text{ cm y}^{-1}$ over the past 100 Myr (Table 1). However, this effect was not included in other runs for two reasons. First, the modern situation is a poor analogue for the past, where \dot{a} was most likely smaller but has large uncertainties (e.g., [Green et al. 2017](#)). Second, tidal dissipation in the Earth-Moon system turned out to have a minor effect on the results compared to other parameters (see Section 3).

2.2. Initial conditions and asteroids

Different sets of initial conditions for the positions and velocities $\chi_0 := (x_0, v_0)$ of the planets and Pluto were employed based on the ephemerides DE431 (released in 2013, [Folkner et al. 2014](#)), DE405 ([Standish 1998](#)), INPOP13c ([Fienga et al. 2014](#)), and INPOP10a ([Fienga et al. 2011](#)). For example, DE431 covers years $-13,200$ to $+17,191$; INPOP13c is available for $J2000 \pm 1,000$ years. The ephemerides are generated by fitting numerically integrated orbits to observations. Ephemeris integrations usually use models of a high degree of completeness and are computationally expensive. One option to obtain initial conditions from ephemerides is by fitting the long-term integration models to ephemerides over a certain time interval (e.g., [Laskar et al. 2011a](#)). It appears that this would modify the initial conditions so as to compensate for the differences between the less complete long-term models and the more sophisticated ephemeris models. Clearly, this approach will lead to improved agreement between the two models

Table 1. Summary of numerical solutions.

Solution	Algorithm	ϵ_{BS} or Δt	Moon	$\mathbf{x}_0, \mathbf{v}_0$	J_2 -rot	Asteroids
ZB17a ^a	BS ^b	1×10^{-15}	separate	DE431	BG05 ^c	10
ZB17b	4th Sympl ^{TT}	0.375 d	ems	DE431	BG05	10
ZB17c	4th Sympl ^{TT}	0.375 d	lun	DE431	BG05	10
ZB17d	2nd Sympl	2.0 d	lun	DE431	BG05	10
ZB17e	2nd Sympl	2.0 d	lun	INPOP13c	BG05	10
ZB17f	2nd Sympl	2.0 d	lun	DE431	HCI ^d	10
ZB17g	2nd Sympl	2.0 d	lun	DE431	BG05	big 3
ZB17h	2nd Sympl	2.0 d	lun	DE431	BG05	8
ZB17i	2nd Sympl	2.0 d	lun	DE431	BG05	13
ZB17j	2nd Sympl	2.0 d	lun	DE431	BG05	16
ZB17k	2nd Sympl	2.0 d	lun,TD ^e	DE431	BG05	10
ZB17p ^p	2nd Sympl	2.0 d	lun	DE431	BG05	10
s405 ^v	2nd Sympl	2.0 d	lun	DE405	–	–
sL11 ^l	2nd Sympl	2.0 d	lun	INPOP10a	BG05	5

^aZB = Zeebe-HNBody.

^bBS = Bulirsch-Stoer.

^cBG05 = Beck & Giles (2005), see Section 2.4.

^{TT} = TipToe HNBody option (extra careful Kepler drifts).

^dHCI = Heliocentric Inertial SPICE frame.

^eTD = Includes tidal dissipation in Earth-Moon system.

^pPlanet 9.

^vTest run for comparison with Varadi et al. (2003)'s R7.

^lTest run for comparison with Laskar et al. (2011b).

over the fit interval. However, will such initial conditions guarantee the most accurate results in the long-term integration across the time intervals not covered by ephemerides? For example, DE431 includes 343 asteroids in the dynamical model, whereas long-term models may include only a few (up to sixteen here) or none at all. Thus, the difference between the long-term- and ephemeris models is of dynamical nature (mutual interactions between Solar System bodies) that persists throughout the entire integration. In contrast, initial conditions affect the positions and velocities of only those Solar System bodies included in the integration and at one particular point in time. Hence the two issues (dynamical model vs. initial conditions) relate to different aspects of the integration, which do not necessarily need to cancel each other out in the long run. Another approach is to directly adopt the initial conditions from ephemerides at an epoch that is covered by modern observations (e.g., Varadi et al. 2003). The latter approach was used here.

For DE431 and DE405 (naif.jpl.nasa.gov/pub/naif/generic_kernels/spk/planets), χ_0 was generated using the SPICE toolkit for Matlab (naif.jpl.nasa.gov/naif/toolkit.html). For INPOP (www.imcce.fr/inpop), χ_0 was generated using the calceph library in C (www.imcce.fr/inpop/calceph). Coordinates were obtained at JD2451545.0 (01 Jan 2000, 12:00 TDB = J2000.0) in certain inertial reference frames and subsequently rotated (cf., Souami & Souchay 2012) if applicable (see Section 2.4). In the following, ICRF

(International Celestial Reference Frame, \equiv J2000 in SPICE) refers to Earth's mean equator and dynamical equinox of J2000.0; ECLIPJ2000 refers to ecliptic coordinates based on the J2000 frame (naif.jpl.nasa.gov/pub/naif/toolkit_docs/C/req/frames.html).

Initial conditions for the asteroids were generated at ssd.jpl.nasa.gov/x/spk.html. All asteroids were treated as heavyweight particles (HWPs) in HNBody, i.e., subject to the same, full interactions as the planets and Pluto. The runs labeled "big 3" (Table 1) include the asteroids Vesta, Ceres, and Pallas. Additional asteroids considered in other simulations were included in the order given in Table 2. The test solution "s405" attempts to replicate simulation R7² of Varadi et al. (2003), who did not include asteroids. The solution "sL11" represents a test run for comparison with Laskar et al. (2011b), including 5 asteroids and initial conditions based on INPOP10a (Fienga et al. 2011).

2.3. Planet 9

The perturbation of a hypothetical Planet 9 (P9) on Earth's eccentricity was examined using one set of orbital elements as proposed in the literature. Note that P9's existence and hence its orbit is entirely speculative at this point (Trujillo & Sheppard 2014; Brown & Batygin 2016; Batygin & Brown 2016; Fienga et al. 2016; Malhotra et al. 2016; Holman & Payne 2016; Shankman et al. 2017; Millholland & Laughlin 2017). Thus, a large array of orbits is possible and the purpose of the current

² Also available at: www2.hawaii.edu/~zeebe/Astro.html

Table 2. Order of asteroids included in different simulations.^a

#	Name	Mass ^b
1	Vesta	1.30E-10
2	Ceres	4.73E-10
3	Pallas	1.05E-10
4	Iris	7.22E-12
5	Bamberg	4.69E-12
6	Hygiea	4.18E-11
7	Euphrosyne	2.14E-11
8	Interamnia	1.78E-11
9	David	1.76E-11
10	Eunomia	1.58E-11
11	Juno	1.22E-11
12	Psyche	1.15E-11
13	Cybele	1.07E-11
14	Thisbe	8.71E-12
15	Doris	8.55E-12
16	Europa	8.37E-12

^aSimulations with N asteroids (see Table 1) include objects #1 to # N .

^bIn solar masses (Folkner et al. 2014).

simulations is merely to test on which time scale a distant perturber would cause a noticeable difference in Solar System trajectories over 100 Myr (see Section 3). P9’s assumed elements/mass were: semimajor axis $a = 654$ AU, eccentricity $e = 0.45$, inclination $I = 30$ deg, longitude of ascending node $\Omega = 50$ deg, argument of perihelion $\omega = 150$ deg, mean anomaly $M = 180$ deg, and mass $m = 10 \times m_{\oplus}$ (Millholland & Laughlin 2017).

2.4. Solar Rotation Axis and Quadrupole Moment J_2

Recent studies have converged on a value for the solar quadrupole moment J_2 of $\sim 2.2 \times 10^{-7}$ (e.g., Pijpers 1998; Mecheri et al. 2004; Fienga et al. 2015; Pitjeva & Pitjev 2014; Park et al. 2017), which was used here throughout. The solar quadrupole moment is directed along the solar rotation/symmetry axis, which is about 6 deg and 7 deg offset from the invariable plane and ECLIPJ2000, respectively (Carrington 1863; Giles 2000; Fränz & Harper 2002; Beck & Giles 2005; Bailey et al. 2016). The initial (Cartesian) coordinates were hence rotated to account for this offset (Souami & Souchay 2012; Fränz & Harper 2002). By default, the quadrupole in HNBody is directed along the z-axis, which was taken as the solar rotation axis. Traditional Carrington elements for inclination and longitude of ascending node of the solar equator relative to ECLIPJ2000 are $i_{\odot} = 7.25$ deg and $\Omega_{\odot} = 75.76$ deg at J2000.0, respectively (Fränz & Harper 2002). However, most runs performed here use more recent values of $i_{\odot} = 7.155$ deg and $\Omega_{\odot} = 75.594$ deg (Beck & Giles 2005) at J2000.0 (labeled BG05 in Table 1). In principle, the coordinate transformation described above is equivalent to expressing the coordinates in the Heliocentric Inertial (HCI) frame in SPICE, except the latter uses the declination $\delta_{\odot} = 63.87$ deg and the right ascension $\alpha_{\odot} = 286.13$ deg of the solar rotation

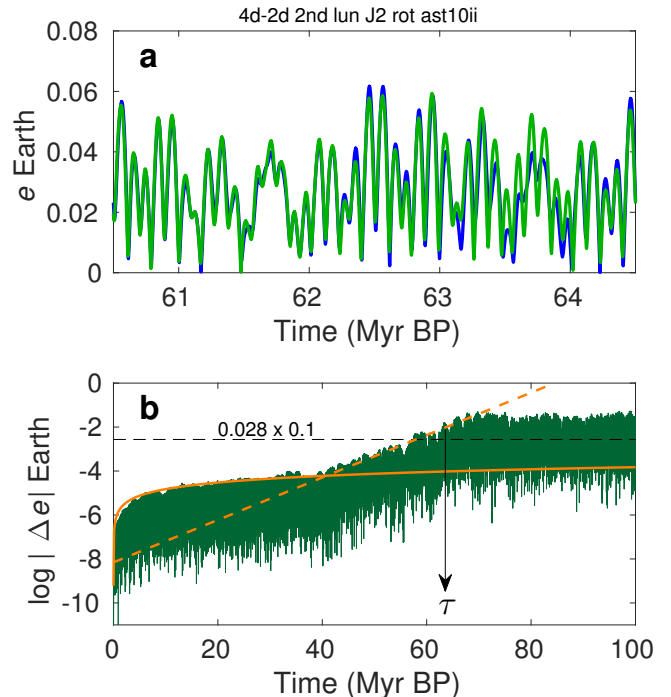


Figure 1. (a) Earth’s orbital eccentricity for the base settings of ZB17d (Table 1) using the HNBody 2nd-order symplectic integrator at $\Delta t = 4$ (green) vs. 2 days (blue). (b) Corresponding difference in Earth’s eccentricity, $|\Delta e_{\oplus}|$, over the past 100 Myr. The arrow indicates the divergence time τ , when $\max|\Delta e_{\oplus}|$ irreversibly crosses $\sim 10\%$ of mean e_{\oplus} ($\sim 0.028 \times 0.1$, dashed line). Orange curves: simple fit functions with linear growth in $|\Delta e_{\oplus}|$ (solid) and exponential growth in $|\Delta e_{\oplus}|$ (dashed, linear on log- y scale) with a Lyapunov time of 4.5 Myr (see text).

axis (solution ZB17f, option J_2 -rot = HCI, Table 1). The s405 setup ($J_2 = 0$) again follows Varadi et al. (2003), who, it appears, did not consider J_2 .

3. RESULTS

In the following, the difference between two orbital solutions will be tracked by the divergence time τ , i.e., the time when the difference in Earth’s eccentricity (Δe_{\oplus}) irreversibly crosses $\sim 10\%$ of mean e_{\oplus} ($\sim 0.028 \times 0.1$, Fig. 1). The divergence time τ as used here should not be confused with the Lyapunov time, which is the time scale of exponential divergence of trajectories and is only ~ 5 Myr for the inner planets (Laskar 1990; Varadi et al. 2003; Batygin & Laughlin 2008; Zeebe 2015a). For the solutions discussed here, the divergence of trajectories is ultimately dominated by exponential growth ($t \gtrsim 40$ Myr BP), which is indicative of chaotic behavior (Fig. 1). Thus, τ is largely controlled by the Lyapunov time, though the two are of course different quantities. Integration errors usually grow polynomially and typically dominate for $t \lesssim 40$ Myr BP (see Fig. 1 and e.g., Varadi et al. (2003)).

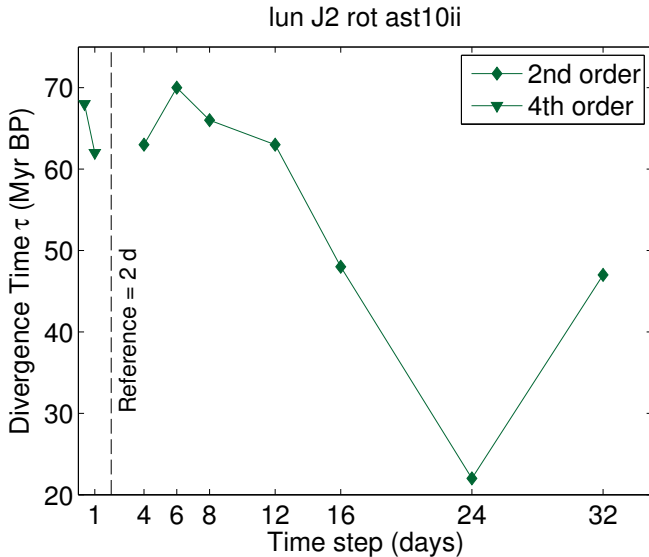


Figure 2. Divergence times for solutions based on the settings of ZB17d (1un option, Table 1) using the HNBody 2nd- and 4th-order symplectic integrator at various time steps, relative to the reference solution obtained at $\Delta t = 2$ days (2nd-order, vertical dashed line). The 4th-order time steps are 0.375 d and 1 d, respectively.

3.1. Numerical algorithm and step size

A given numerical algorithm is often evaluated by varying its accuracy or step size (Δt), while keeping all other parameters constant. For instance, for the base settings of ZB17d (Table 1), HNBody’s 2nd-order symplectic integrator gives $\tau \simeq 63$ Myr at $\Delta t = 4$ vs. 2 days (Fig. 1). One might hence assume that τ reflects the time span of the validity of the symplectic solution when using progressively smaller step sizes and that τ would drop off rapidly for larger Δt . However, this is not necessarily the case, as test runs with the ZB17d setup (1un option) and different Δt show (Fig. 2). Using $\Delta t = 2$ d as the reference case, the symplectic runs with larger time steps of 4, 6, 8, and 12 days all show **larger** τ ’s than with a smaller time step of 1 day, which appears counterintuitive. One might expect **smaller** τ ’s at larger time steps (supposedly less accurate). Only for $\Delta t \gtrsim 12$ d, τ starts to fall off. Surprisingly, even for an absurdly large time step of 32 days, the symplectic solution only diverges from the reference case with 2-day time step at ~ 47 Myr (Fig. 2, all 1un option). These results suggest that the relationship between divergence time and time step is not a robust indicator for the accuracy of symplectic solutions.

Moreover, integrations with different algorithms (symplectic vs. Bulirsch-Stoer at small $\Delta t = 0.375$ d and relative accuracy $\epsilon_{\text{BS}} = 1 \times 10^{-15}$, respectively) diverge at ~ 63 Myr (Fig. 3). This is earlier than some solutions obtained with just a single algorithm, e.g., the symplec-

tic integrations for $\Delta t = 2$ vs. 6 days discussed above ($\tau \simeq 70$ Myr). Hence, while symplectic integrations with 1un option appear internally remarkably consistent at different time steps, this does not necessarily imply that symplectic solutions are reliable up to τ , as the comparison with a different algorithm shows. At this stage, it remains inconclusive which numerical algorithm provides more accurate solutions for the problem at hand.

For example, the most expensive simulation of the present study, i.e., the 4-month-long BS integration (ZB17a) at relative accuracy $\epsilon_{\text{BS}} = 1 \times 10^{-15}$ shows excellent conservation of energy and angular momentum ($\max|\Delta E/E| \lesssim 3 \times 10^{-13}$, $\max|\Delta L_z/L_z| \lesssim 5 \times 10^{-12}$, Fig. 3). This is an important consideration for BS-integrations, which suffer from significant E - and L -drifts if the time step is too large. However, E and L_z are nearly equally well preserved in the 4th-order symplectic integration ZB17c with the smallest time step used ($\Delta t = 0.375$ d, Fig. 3). Thus, energy- and angular momentum conservation do not provide a criterion here for selecting one solution/algorithm over the other.

Establishing quality criteria just among symplectic integrators based on energy properties also appears elusive. Usually, the long-term energy drift and fluctuations around the short-term mean increase with the symplectic step size. For example, the symplectic $\Delta t = 12$ d-run has $\sim 100\times$ and $\sim 10\times$ larger standard deviation and energy drift, respectively, than the $\Delta t = 0.375$ d-run (ZB17c, Fig. 2). One might therefore assume the ZB17c solution to be more accurate. However, both symplectic solutions (0.375 d and 12 d time step) diverge from ZB17a at ~ 63 Myr, providing no conclusion about accuracy. Furthermore, this leads to the bizarre conclusion that the 4-month Bulirsch-Stoer integration and the 5-hour (wall-clock time) symplectic integration with 1un option at $\Delta t = 12$ d give essentially the same results to ~ 63 Myr. Thus, full Solar System integrations for, e.g., parameter studies over $\lesssim 60$ Myr may be completed within a few hours, rather than months.

3.2. Test against previous solutions

Further insight into the behavior of numerical orbital solutions may be gained by testing whether previous simulations can be reproduced when the same assumptions for the underlying physical model of the Solar System are used. For example, Varadi et al. (2003) (V03 for short) used a Störmer scheme to integrate the orbits of the major planets over the past 207 Myr (their simulation R7), including GR corrections. V03’s initial conditions were taken from DE405 (Standish 1998), while the Moon’s influence on the net motion of the Earth-Moon barycenter was modeled in R7 via a mean quadrupole potential with a correction factor $f_{1\text{un}} = 0.8525$. Based on the information provided in V03, effects of J_2 and as-

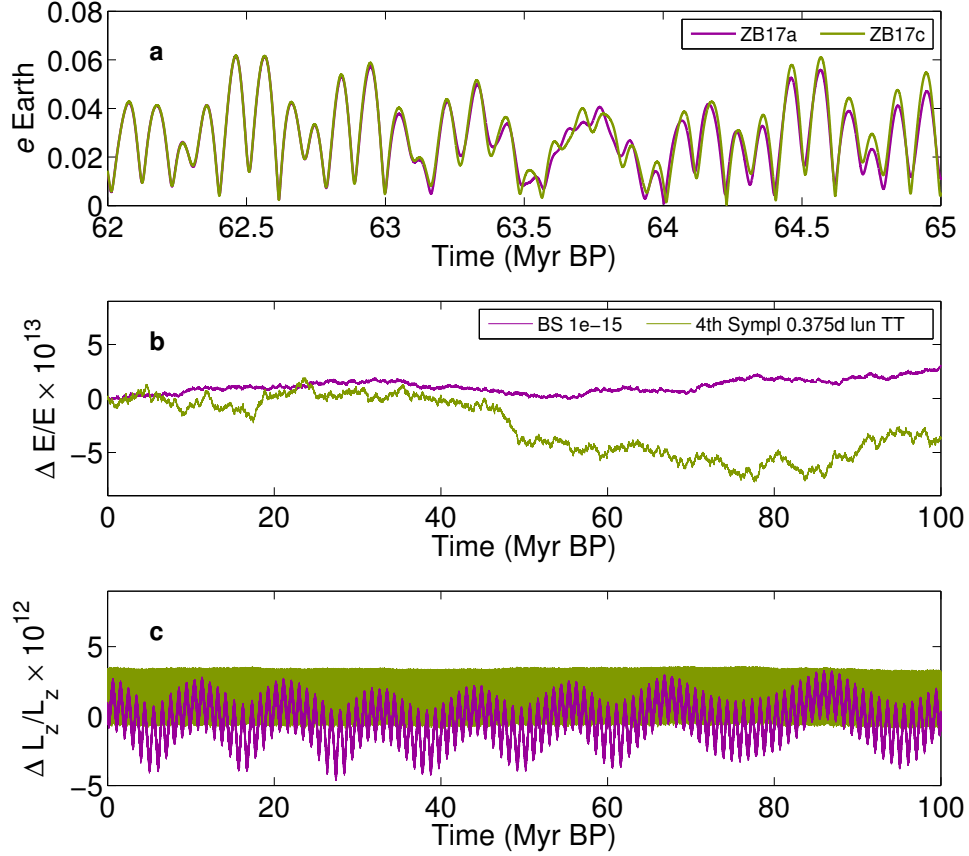


Figure 3. (a) Solutions ZB17a (Bulirsch-Stoer, purple) and ZB17c (symplectic, green). Maximum relative error in (b) total energy $|\Delta E/E| = |(E(t) - E_0)/E_0|$ and (c) in z-component of angular momentum ($|\Delta L_z/L_z|$). Note that steps in the symplectic energy due to close encounters of asteroids have been removed. TT = TipToe HNBODY option (extra careful Kepler drifts).

teroids were not included in the computations.

The current test simulation s405 (Table 1) uses the same physical model as V03 but was integrated using HNBODY’s 2nd-order symplectic integrator with $\Delta t = 2$ days. Solutions s405 and V03-R7 diverge at $\tau \simeq 54$ Myr (Table 3, Fig. 4). This result is encouraging in terms of reproducibility, given that different integrator algorithms were used and the fact that several other pairs of solutions diverge earlier (Table 3).

Using the Solar System model and symplectic integrator from the long-term solution La10 (Laskar et al. 2011a), Laskar et al. (2011b) provided orbital solutions over the past 100 Myr (La11 for short). Initial conditions were based on INPOP10a (Fienga et al. 2011; Westendorp et al. 2012) and the Moon plus 5 asteroids (Ceres, Pallas, Vesta, Iris, and Bamberga) were included as separate, full-interacting objects. The present test solution sL11 uses a similar setup but uses the lun option and HNBODY’s 2nd-order, 2-day step integrator (Table 1). The solar rotation axis and quadrupole moment were included as described in Section 2.4 using the BG05 option. The solutions sL11 and La11 diverge at ~ 47 Myr

(Table 3, Fig. 4) and hence notably earlier than for the Varadi et al. (2003) test case. The reason could be differences in setup and integrator, as mentioned above. Interestingly, when 10 asteroids are included, the solution ZB17b, for instance, stays closer to La11 than sL11 ($\tau \simeq 50$ Myr, Table 3, Fig. 5).

3.3. Orbital solutions ZB17a,b,c

The orbital solutions ZB17a,b,c are based on the most expensive integrations presented here (Table 1, Fig. 5). Remarkably, while the BS option (ZB17a) and the symplectic lun option (ZB17c) diverge at ~ 63 Myr, the ems option separates much earlier, ~ 54 Myr (Table 3). The difference between ZB17b and ZB17c is the treatment of the Earth-Moon system (all else being equal, see Section 2). The ems option uses a symplectic sub-integration of the Earth-Moon-Sun system, while the lun option is based on a simple quadrupole perturbation. One potential explanation for ZB17b’s early separation is that the ems option as implemented gives a less accurate lunar orbit at constant step size $\Delta t = 0.375$ d than the BS option with adaptive step size con-

Table 3. Selected, approximate divergence times (τ in Myr BP) for pairs of solutions \mathcal{S}_{ij} .

\mathcal{S}^s	a	b	c	d	e	f	g	h	i	j	k	p	V03 ^v	La11 ^l	La04 ^m
a		54	63	63									41	50	41
b			54	54									41	50	41
c				68									41	50	41
d					54	63	48	56	54	54	63	65			
s405													54		
sL11														47	

^s Solutions, see Table 1: a = BSe-15, b = 0.375d.ems, c = 0.375d.lun, d = 2nd2d.lun, e = inpop13c, f = hci, g = big3, h = ast8, i = ast13, j = ast16, k = tidal-dissipation, p = Planet 9.

^v Varadi et al. (2003), run R7.

^l Laskar et al. (2011b). $\tau(\text{ZB17a-La10x}) = [41 \ 50 \ 50 \ 50]$, where $x = a, b, c, d$.

^m Laskar et al. (2004).

trol (ems and BS both treat the Moon as a separate object). The lun option (ZB17c) with a correction factor $f_{\text{lun}} = 0.8525$ (Quinn et al. 1991; Varadi et al. 2003; Rauch & Hamilton 2002) happens to agree with the BS option (ZB17a) between ~ 54 Myr and ~ 63 Myr. In the following, the lun option will be preferred over the ems option. Note, however, that the relative agreement between ZB17a and ZB17c does not prove superior absolute accuracy of these solutions over others.

3.4. Orbital solutions ZB17d-p

The solutions ZB17d-p provide tests of various parameters (Table 1). The basic setup for all these runs follows ZB17d using the 2nd-order, 2-day, symplectic integrator with lun option. ZB17d diverges from ZB17a (BS) and ZB17c (the more expensive symplectic version) at $\tau \simeq 63$ Myr and $\tau \simeq 68$ Myr, respectively (Table 3), lending confidence to the general performance of the ZB17d setup for $t \lesssim 63$ Myr. Importantly, the simulations showed that ZB17e and ZB17d, which use initial conditions from INPOP13c and DE431, respectively, diverge already at ~ 54 Myr. It is not clear at this time which of these ephemerides is more accurate. Thus, the uncertainty in ephemerides currently appears to be one major limitation for identifying a unique orbital solution beyond ~ 54 Myr (see discussion, Section 5).

ZB17f uses a minimally different orientation for the solar rotation axis, which has a minor effect, as $\tau \simeq 63$ Myr relative to ZB17d (Table 3). On the contrary, including only the big 3 asteroids (ZB17g) instead of 10 asteroids (ZB17d), drops τ to ~ 48 Myr, indicating a significant influence of asteroids on the system's dynamic, despite their small mass (cf., Laskar et al. 2011b). Relative to ZB17d, τ increases from 48 to 56 Myr when the number of asteroids (N) grows from 3 to 8, but drops to 54 Myr for $N = 13$ and 16, respectively. This rep-

resents another major limitation to finding a unique orbital solution beyond ~ 54 Myr (Section 5). Tidal dissipation in the Earth-Moon system, as well as a hypothetical Planet 9 appear to have minor effects on the results (ZB17k and ZB17p, $\tau \simeq 63$ and 65 Myr, respectively).

Finally, note that using τ as a criterion, the current state-of-the-art solutions (which include ZB17a-p but g) all differ from previously published results beyond ~ 50 Myr (Table 3). The solutions ZB17a-p, as well as La11, diverge from La04 at ~ 41 Myr. At the core of the divergence of the different orbital solutions lies the Solar System's chaotic behavior, i.e., the sensitivity to initial conditions and tiny perturbations (see Section 5). To provide some insight into the origin of the chaos, an eigenmode analysis will be presented in the next section. We return to the discussion of the various orbital solutions in Section 5.

4. EIGENMODE ANALYSIS

If the mutual planet-planet perturbations were sufficiently small (all eccentricities and inclinations small), then the full dynamics of the Solar System could be described by linear secular perturbation theory, aka Laplace-Lagrange solution (e.g. Morbidelli 2002; Malhotra 2012). The existence of chaotic trajectories, however, shows that this is not the case. To understand the nature of higher-order perturbations, it is instructive to examine the difference between solutions of the full system (numerical) and the linear Laplace-Lagrange solution (analytical) (e.g. Applegate et al. 1986; Nobili et al. 1989; Laskar 1990). From the numerical solution of the planets and Pluto ($i = 1, \dots, 9$), the fundamental frequencies were obtained by time-series analysis of the classical variables:

$$h_i = e_i \sin(\varpi_i) \quad ; \quad k_i = e_i \cos(\varpi_i) \quad (1)$$

$$p_i = \sin(I_i/2) \sin(\Omega_i) \quad ; \quad q_i = \sin(I_i/2) \cos(\Omega_i) \quad (2)$$

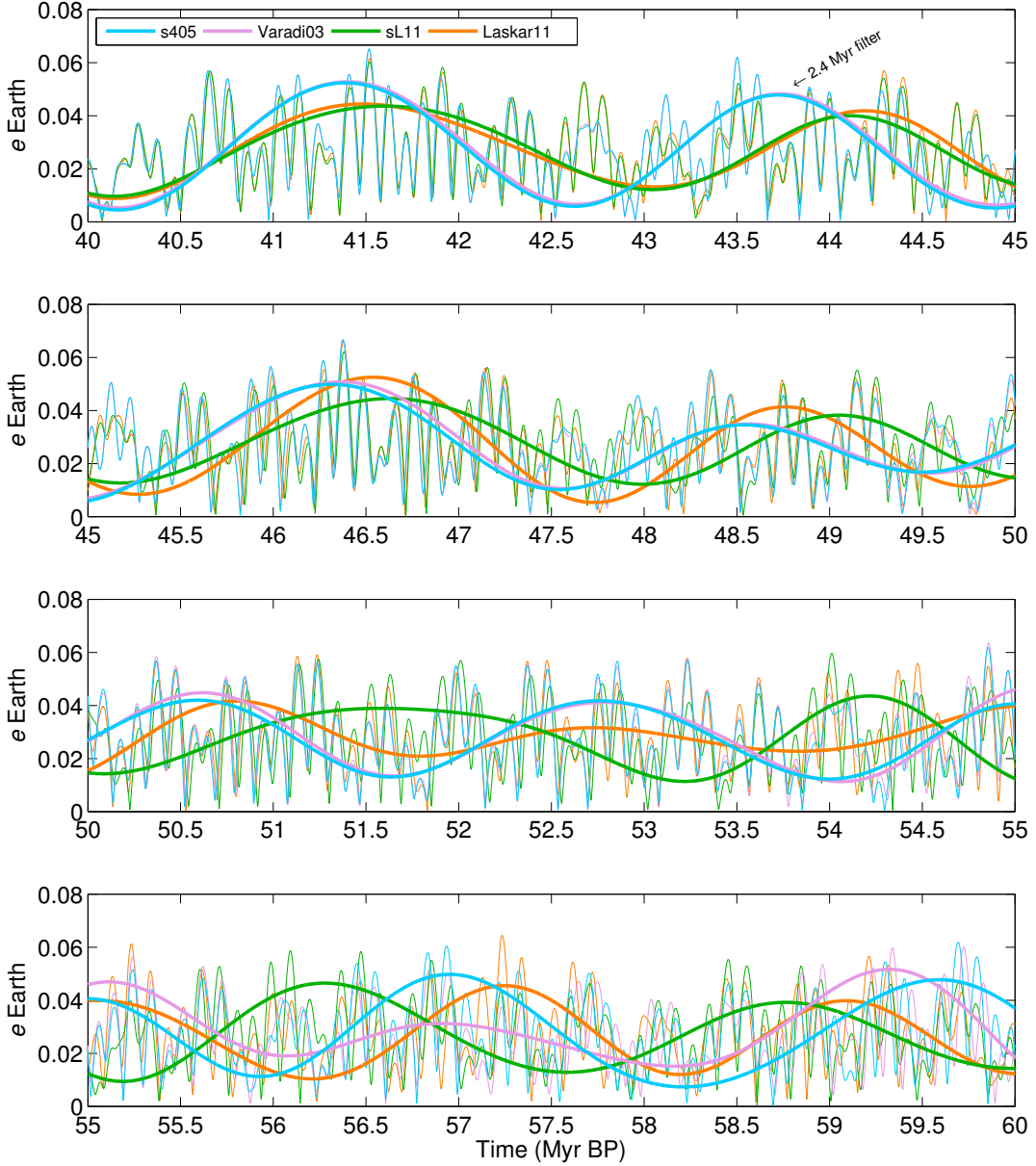


Figure 4. Comparison of Earth’s computed eccentricity (thin lines) of previously published and current test solutions. For labels and features of different solutions, see text and Tables 1 and 3. Also, a ~ 2.4 -Myr Gaussian filter was applied to all solutions to aid in identifying differences in the low-frequency range around $g_4 - g_3$ (thick lines, arbitrary scaling). Gaussian filter parameters are: $\sigma = df / \sqrt{2 \ln(2)}$ with half-width $df = 0.5 \cdot f$; i.e., bandwidth $f \pm 50\%$ where $f = 0.4209 \text{ Myr}^{-1}$.

where e , I , ϖ , and Ω are eccentricity, inclination, longitude of perihelion, and longitude of ascending node, respectively. The frequencies were computed using a zero-padded FFT over the time interval 0 to 20 Myr BP (Table 4) and agree well with La10 (Laskar et al. 2011a). The largest differences were found for g_1 and s_1 ($\sim 0''.008 \text{ yr}^{-1}$ and $\sim 0''.005 \text{ yr}^{-1}$, respectively). The frequency s_5 is zero because of angular momentum conservation (invariable plane).

It is important to recall that there is no simple one-to-one relation between planet and eigenmode, partic-

ularly for the inner planets. The system’s motion is a superposition of all eigenmodes, although some modes represent the single dominant term for some (mostly outer) planets. Assume that each h, k and p, q from the numerical solution can be approximated as a linear combination of the eigenmodes associated with g_j and s_j plus higher-order terms (ellipses):

$$h \simeq \sum A_j \sin(g_j t + \Phi_j) + \dots \quad (3)$$

$$k \simeq \sum A_j \cos(g_j t + \Phi_j) + \dots \quad (4)$$

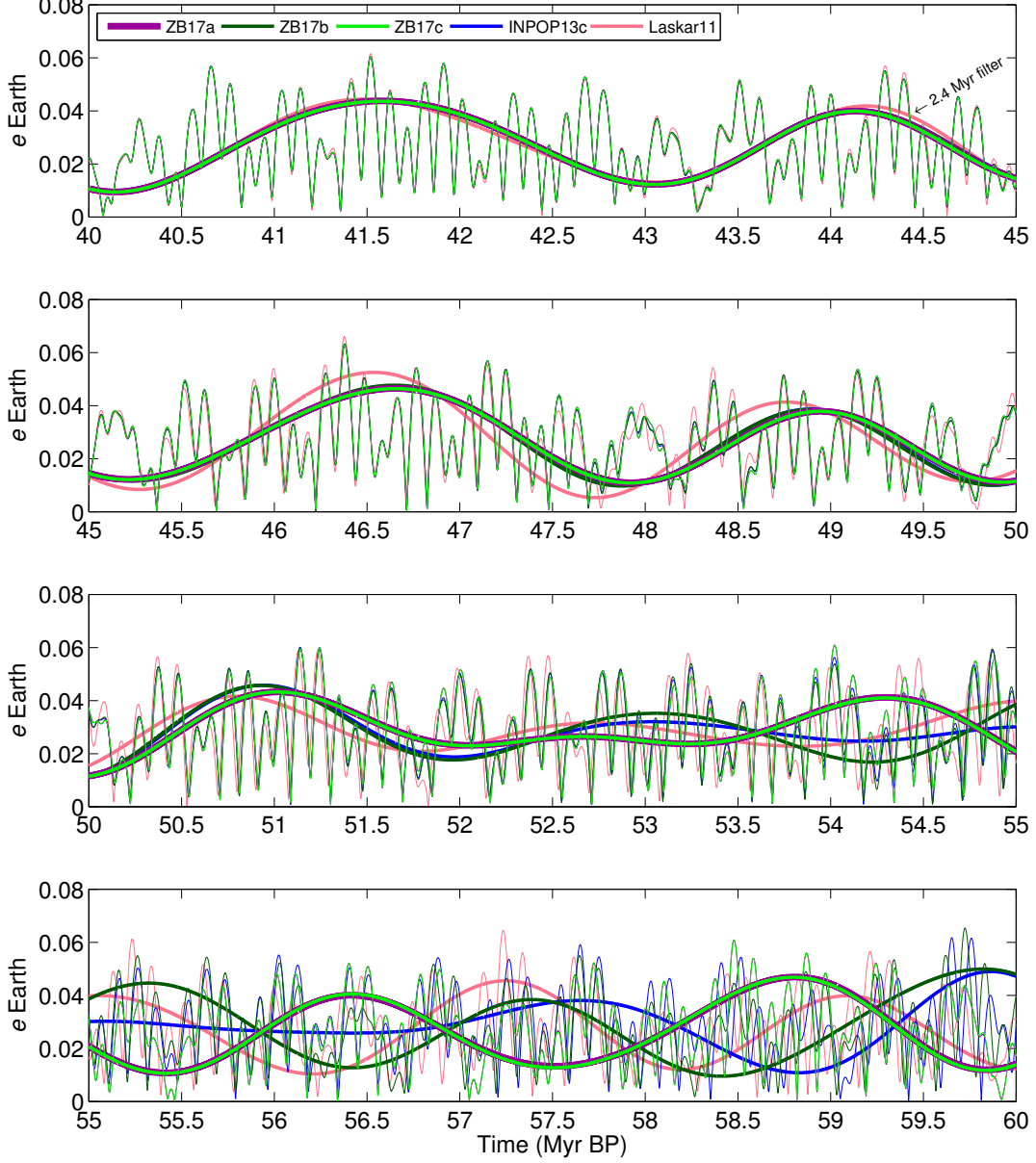


Figure 5. Earth’s computed eccentricity (thin lines) of selected current solutions and La11. For details, see text and Tables 1 and 3. Gaussian filter (thick lines) as in Fig. 4 with arbitrary scaling. Solutions ZB17a and ZB17c agree to 63 Myr, thus ZB17a’s line width (purple, filtered) was increased for visibility. Note that for, e.g., La11-ZB17c (Table 3), the definition of τ (cf., Fig. 1) gives a divergence time of ~ 50 Myr, while the filtered La11 curve could connote a slightly extended agreement. However, La11 and ZB17c are irreversibly out-of-phase beyond ~ 50 Myr, which causes $\max|\Delta e_{\mathcal{E}}|$ to cross the threshold.

$$p \simeq \sum B_j \sin(s_j t + \Psi_j) + \dots \quad (5)$$

$$q \simeq \sum B_j \cos(s_j t + \Psi_j) + \dots, \quad (6)$$

where A_j and B_j are amplitudes, and Φ_j and Ψ_j are phases. In the full nonlinear system, the g ’s and s ’s may change over time. In contrast, in the linear Laplace-Lagrange (LL) solution, the fundamental frequencies are constant and higher-order terms are absent. Hence a comparison over, say, 100 myr of the full solution (Eqs. (1) and (2)) vs. the linear solution (LL-version of

Eqs. (4) and (6)) might provide some insight into the chaotic behavior of the full system (e.g., Laskar et al. 2011a). LL-version here means no higher terms and constant frequencies, amplitudes, and phases (say, obtained from a fit over 20 Myr).

For example, in the linear case (denoted by ** in the following; i.e., no higher terms in Eqs. (4) and (6)), we can lump all h^* into a vector \mathbf{h}^* ($i = 1, \dots, 9$) and write:

$$\mathbf{h}^* = A \mathbf{u}^*, \quad (7)$$

Table 4. Fundamental frequencies (arcsec yr⁻¹) and periods (yr) of the Solar System over 20 Myr from ZB17c.

#	g ("yr ⁻¹)	T_g (yr)	s ("yr ⁻¹)	T_s (yr)	g_{La10}^a ("yr ⁻¹)	s_{La10}^a ("yr ⁻¹)
1	5.5821	232,170	-5.6146	230,829	5.59	-5.61
2	7.4559	173,821	-7.0629	183,493	7.453	-7.06
3	17.3695	74,613	-18.8476	68,762	17.368	-18.848
4	17.9184	72,328	-17.7492	73,017	17.916	-17.751
5	4.2575	304,404	0.0000	-	4.257482	0
6	28.2452	45,884	-26.3478	49,188	28.2449	-26.347841
7	3.0878	419,719	-2.9926	433,072	3.087946	-2.9925258
8	0.6736	1,923,993	-0.6921	1,872,457	0.673019	-0.69174
9	-0.3494	3,709,721	-0.3511	3,691,356	-0.35007	-0.35

^a La10's g and s for comparison (Laskar et al. 2011a).

where A is a matrix of amplitudes and $u_j^* = \sin(g_j t + \Phi_j)$. For $\det(A) \neq 0$, this can be inverted to give $u^* = A^{-1} h^*$. For the full system, we may write a similar expression at each time step, $u(t) = A^{-1} h(t)$. However, due to higher-order terms, the amplitudes of the u_j will differ from 1 and the frequencies will no longer be constant. Thus, the deviation of u from u^* (simple sinusoids) provides a measure of the importance of the higher-order perturbations in the g -modes (correspondingly v from v^* with matrix B in the s -modes, see p -variable above).

For $j = 5, \dots, 9$ (dominant in outer planets), the u and v amplitudes are close to 1 (not shown), but not for $j = 1, \dots, 4$ (dominant in inner planets, Fig. 6). The largest amplitude variation in g -modes occurs in u_3 and u_4 . Also, u_3 's and v_3 's long-term pattern differ between the interval 0-50 Myr vs. 50-100 Myr; a similar pattern shift occurs in u_4 and v_4 (though not visible in the figure). Such a shift is not apparent in u_1 , u_2 , v_1 , and v_2 . The largest amplitude variation in s -modes occurs in v_2 . As expected, these observations suggest that higher-order terms are critical for the inner planets. In addition, an apparent change in eigenmodes occurs around 50 Myr BP in the solution ZB17c (as well as in other solutions, not shown). This point in time corresponds to the time of change in secular trends of the arguments $\Delta\Theta_3$ and $\Delta\Theta_4$ (see Fig. 7).

Changes in the frequencies and phases of the full solution (constant in the linear case) may be examined by comparing the arguments of u and u^* . For the latter, we may simply take $g_j t + \Phi_j =: \Theta_j^*$ and $s_j t + \Psi_j =: \Lambda_j^*$ as arguments. For the full solution, a complex variable will come in handy, which can be defined in the linear case as ($i = \sqrt{-1}$):

$$z_j^* = \mu_j^* + i u_j^* = \cos(\Theta_j^*) + i \sin(\Theta_j^*) = e^{i\Theta_j^*}, \quad (8)$$

where $\mu^* = A^{-1} k^*$ and $u^* = A^{-1} h^*$. By analogy, we

compute u 's arguments from:

$$z_j = \mu_j + i u_j \quad (9)$$

where $\mu(t) = A^{-1} k(t)$ and $u(t) = A^{-1} h(t)$. Hence, the arguments of the g -eigenmodes for the full solution can be calculated as $\Theta_j = \arctan 2(u_j, \mu_j)$. In the linear case, the arguments Θ_j^* and Λ_j^* simply represent straight lines as a function of time with slopes g_j and s_j , respectively. Frequency and phase changes in the full solution will therefore cause deviations from zero in the variables $\Delta\Theta_j = \Theta_j - \Theta_j^*$ and $\Delta\Lambda_j = \Lambda_j - \Lambda_j^*$.

The g -arguments Θ_5 and Θ_6 (dominant in Jupiter and Saturn), show negligible secular trends over 100 Myr, that is, g_5 and g_6 are nearly constant, as in the linear case ($\Delta\Theta_5$ and $\Delta\Theta_6 \lesssim 0.05$ rad, Fig. 7a). On the contrary, secular trends in $\Delta\Theta_3$ and $\Delta\Theta_4$ before ~ 40 Myr are typically much larger (for various solutions including ZB17c, see Fig. 7a). For example, $d(\Delta\Theta_3)/dt \simeq 30$ rad/50 Myr in ZB17c between 40 and 90 Myr (Fig. 7a), or 6×10^{-4} rad kyr⁻¹. If arguments are given as $2\pi\hat{g}t$, where \hat{g} is in kyr⁻¹ and t in kyr, then the corresponding frequency change is $\Delta\hat{g} = d(\Delta\Theta)/dt/2\pi$, hence $\Delta\hat{g}_3 \simeq 9.5 \times 10^{-5}$ kyr⁻¹. A FFT analysis of \hat{g}_3 over consecutive 20-Myr intervals spanning the full 100 Myr indicates a maximum change of $\sim 8 \times 10^{-5}$ kyr⁻¹ in \hat{g}_3 , corroborating the secular trend observed in $\Delta\Theta_3$.

The rapid shift in $\Delta\Theta_3$ around 89 Myr (Fig. 7a, arrow), however, is not related to a frequency change. Such shifts in arguments can occur at the nodes of the eigenmodes, where the u - or v -amplitude becomes small and the calculated argument changes rapidly. For example, the $\Delta\Theta_3$ -shift coincides with a node in u_3 at 89 Myr (Fig. 6, arrow). In this case, small variations in u_3 's and μ_3 's amplitudes lead to an apparent rapid phase shift between u_3 and μ_3 . The offset in $\Delta\Theta_3$ between ~ 1 Myr prior to, and immediately after the shift amounts to $\sim 4\pi$; otherwise $\Delta\Theta_3$ remains fairly constant across the

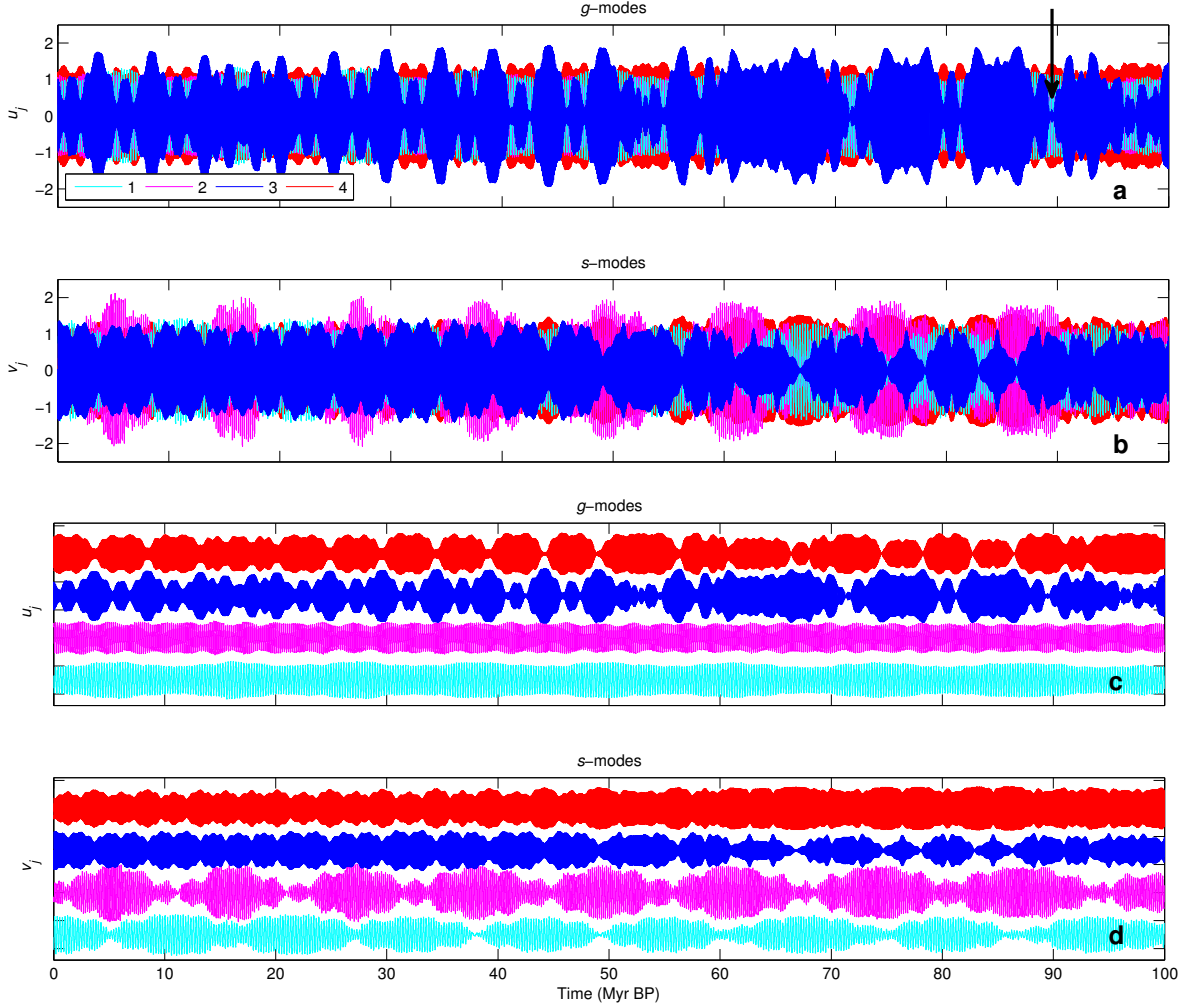


Figure 6. (a) Eigenmode components u_j and (b) v_j for $j = 1, \dots, 4$ corresponding to g - and s -modes (for frequencies, see Table 4). (c) u_j and (d) v_j plotted with arbitrary offsets for clarity. Note the large amplitude variations in e.g., u_3 , v_3 and the change in pattern around 50 Myr BP, (cf. time of change in secular trends of the arguments $\Delta\Theta_3$ and $\Delta\Theta_4$, Fig. 7). The arrow at 89 Myr in (a) indicates a node in u_3 associated with a rapid change in argument (see Fig. 7).

~ 6 Myr interval centered on the shift. Similar shifts occur in the arguments related to g_4 (Fig. 7a), s_1 , and s_2 (Fig. 7b). Before ~ 40 Myr, secular trends are visible in the arguments $\Delta\Lambda_3$ and $\Delta\Lambda_4$, associated with s_3 and s_4 .

4.1. An expression of chaos

Given that the values of g_3 and g_4 are close to one another and that both the amplitudes and arguments of u_3 and u_4 show the largest variations (and hence deviations from the linear solution) suggests that these modes are strongly involved in the system's chaotic behavior (cf., Laskar 1990). It also turned out that the difference in g -arguments between two different solutions ($\Theta_j - \Theta'_j$) grows most rapidly around the eccentricity divergence time, τ , for $j = 3, 4$ than for other values of j . This is not necessarily the case for s -arguments $\Lambda_j - \Lambda'_j$ (note that divergence times for eccentricity and inclination are

very similar). For ZB17b vs. ZB17c, for example, the eccentricity- τ is ~ 54 myr. At ~ 53 Myr, the difference in the g -arguments $\Theta_3 - \Theta'_3$ increases rapidly for these two solutions (Fig. 8a).

The g -modes are related to both the planets' orbital eccentricities and longitudes of perihelia (ω 's). Examination of ω and ω' for two different solutions close to the divergence time revealed a first occurrence of branching into two fundamentally different physical trajectories for either Venus', Earth's, or Mars' orbit. For example, ω_E (ZB17b) circulates at 52.71 Myr, whereas ω'_E (ZB17c) librates (Fig. 9). While libration and circulation occur constantly across the entire time span, the juncture at 52.71 Myr is the first (youngest) occurrence when ω_E and ω'_E take opposite paths (ω -branching of the two solutions, illustrated in Fig. 10). Branching occurs frequently in the time interval before ~ 53 Myr (older). In

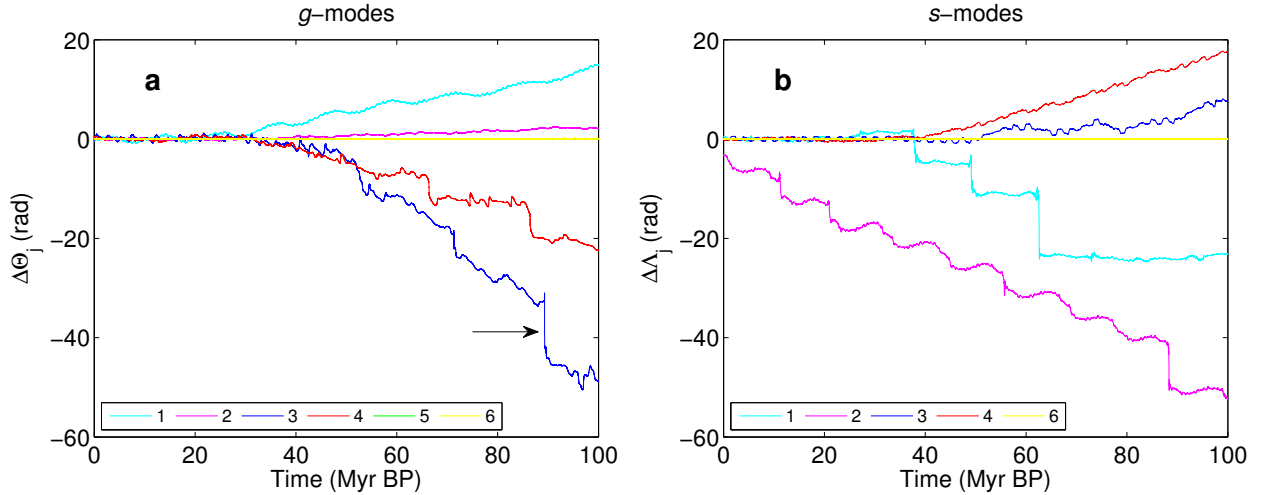


Figure 7. Differences in arguments (a) $\Delta\Theta_j = \Theta_j - \Theta_j^*$ and (b) $\Delta\Lambda_j = \Lambda_j - \Lambda_j^*$ (in radians) associated with g - and s -eigenmodes between the full numerical solution and the linear case for $j = 1, \dots, 6$ (except for $s_5 = 0$, see text). The arrow at 89 Myr in (a) indicates a rapid change in argument associated with a node in u_3 (see Fig. 6).

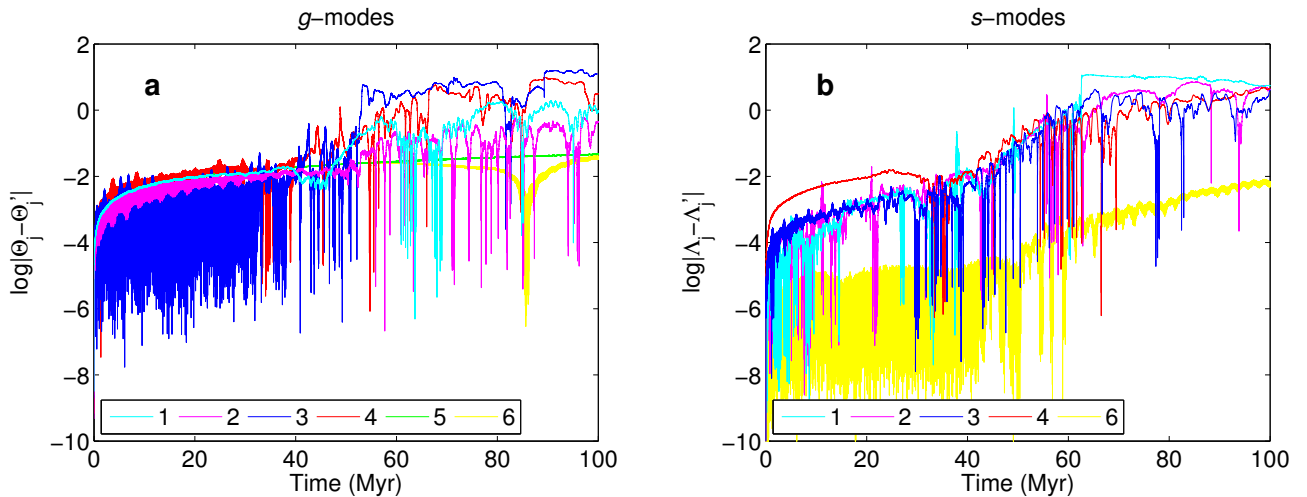


Figure 8. Example of the difference in arguments between two solutions (ZB17b and ZB17c). (a) $\log|\Theta_j - \Theta'_j|$ and (b) $\log|\Lambda_j - \Lambda'_j|$ associated with g - and s -arguments, respectively.

the current example, the first ω -branching is described for Earth's orbit and coincides closely with the rapid rise in $\Theta_3 - \Theta'_3$ at ~ 53 Myr (Fig. 8a). However, this is not always the case. The first branching may occur somewhere around τ for either Venus', Earth's, or Mars' orbit. It is likely that the preconditioning of ω for circulation vs. libration at junctures such as the one illustrated in Figs. 9 and 10 is sensitive to small differences in initial conditions (and/or minuscule perturbations) and would therefore represent an expression of the chaotic nature of the inner Solar System.

5. DISCUSSION

The comparison of the current test solutions against published orbital solutions (Section 3.2) provides some insight into how different numerical realizations compare between different investigator groups using different codes and integrator packages (external comparison). The agreement between Varadi et al. (2003)'s R7-run and the current test solution s405 shows reproducibility to ~ 54 Myr BP (Fig. 4), despite the fact that two different integrator algorithms were used. The comparison between Laskar et al. (2011b) and the sL11 test-solution is slightly less encouraging (Fig. 4). However, when 10 asteroids are included instead of 5, the

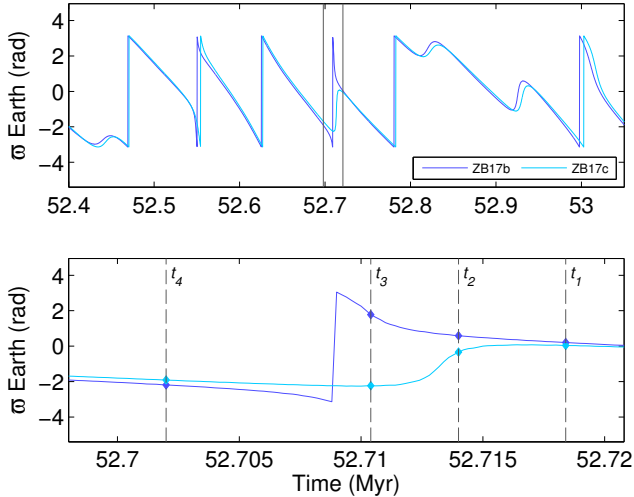


Figure 9. Longitude of perihelion ω (ZB17b) and ω' (ZB17c) for Earth’s orbit around 52.7 Myr. Note different time axes in top and bottom panel. For illustration of orbits at times t_1 to t_4 , see Fig. 10. Note that the branching of ω and ω' for the two solutions is easy to spot here because ω crosses from $+\pi$ to $-\pi$ close to t_3 . Otherwise, branching may be more difficult to identify but only occurred at times older than τ .

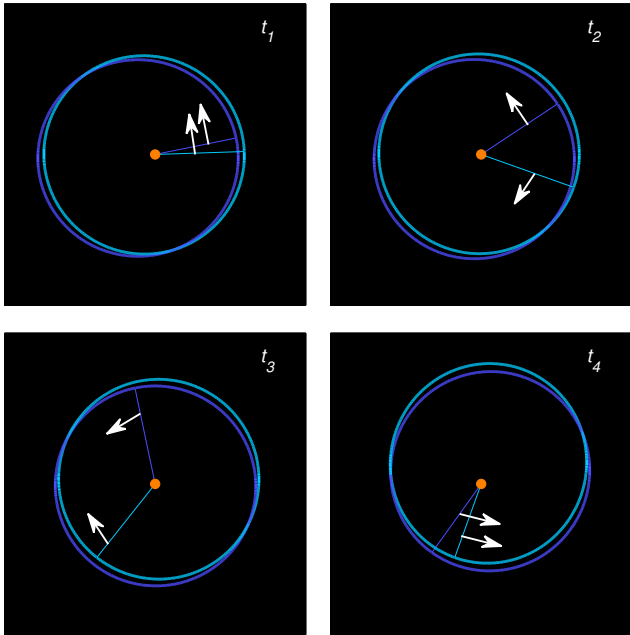


Figure 10. Illustration of Earth’s orbit at times t_1 to t_4 for ZB17b (blue) and ZB17c (cyan) corresponding to Fig. 9. For visualization, the eccentricity of Earth’s orbit has been exaggerated. Straight colored lines fall along lines of apsides (connecting to perihelia). Arrows indicate the direction of apse line rotation.

agreement improves (Fig. 5). The current state-of-the-art solutions agree with La10x ($x = a,b,c,d$) and La11 up to ~ 50 Myr (Table 3). On the one hand, this is en-

couraging because it suggests validity of the solutions over that time period. On the other hand, the disagreement beyond ~ 50 Myr poses a potential challenge because the source for the discrepancy is unclear at this point. It could reflect a minor issue such as small differences in setup parameters and initial conditions, but could also reflect differences in numerical integrators.

The symplectic integrations at different time steps (Fig. 2) showed astonishing consistency, even at absurdly large step sizes, which leads to at least two important conclusions. First, the relationship between time step and divergence time is not a robust indicator for the absolute accuracy of symplectic integrations. Second, the symplectic integration with 1 μ n option and 12-day time step (5-hours wall-clock time) and the 4-month Bulirsch-Stoer integration diverge only at ~ 63 Myr. Thus, full Solar System integrations, say, for parameter studies over $\lesssim 60$ Myr may be completed within a few hours, rather than months.

The current study provides new state-of-the-art orbital solutions for applications in geological studies. ³ The solutions ZB17a and ZB17c agree to ~ 63 Myr, despite the fact that two fundamentally different integrator algorithms were used. The agreement between ZB17a and ZB17c extends ~ 9 Myr beyond that with ZB17b, possibly due to the *ems* option used in ZB17b (see Section 3.3). Also, ZB17a,b,c represent the most expensive Bulirsch-Stoer- and symplectic integrations (smallest error per step and smallest symplectic time step, Table 1). It is hence conceivable that ZB17a and ZB17c are the most accurate solutions provided here that are based on DE431 initial conditions (see discussion below though). However, the relative agreement between ZB17a and ZB17c does not prove superior absolute accuracy of these solutions over others. Also, inferring accuracy from step size and energy properties of symplectic integrators is problematic (see Section 3.1).

Given the chaotic nature of the system (see Section 4), the uncertainty in ephemerides (e.g., difference between DE431 and INPOP13c) currently appears to be one major limitation for identifying a unique orbital solution beyond ~ 54 Myr. The number of asteroids (N) included in the simulations represents another major limitation. One might expect that once a certain number of asteroids has been included, the divergence time τ would remain constant, as the effect of asteroid mass on the system’s dynamic would approach a limit. However, this is not the case. For example, while relative to ZB17d ($N = 10$), τ does increase from 48 to 56 Myr when N grows from 3 to 8, τ drops to 54 Myr for $N = 13$ and 16, respectively (Table 3). Given $\tau = 54$ Myr, asteroids

³ Numerical solutions are freely available at: www2.hawaii.edu/~zeebe/Astro.html

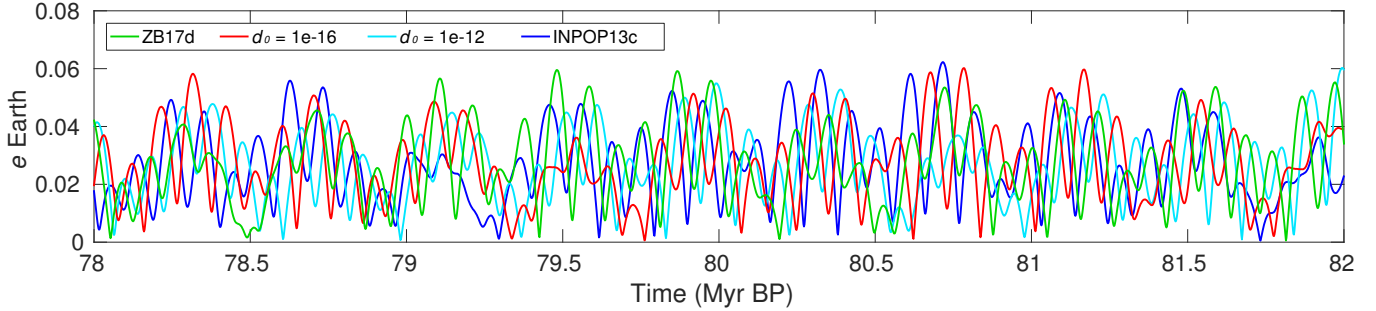


Figure 11. Illustration of solutions obtained with the same setup and integrator as ZB17d (DE431), except for small differences in initial conditions. Time interval shown is sufficiently beyond divergence time. Values for d_0 indicate difference to DE431 in Earth’s x -coordinate. Initial conditions from INPOP13c were applied to all planets and Pluto.

therefore represent a similarly limiting factor as initial conditions.

5.1. Constraints from geologic records

Can geologic evidence help to constrain astronomical solutions further back in time? For example, one approach currently pursued is to search for and identify chaotic resonance transitions in geologic records (occurring at specific ages), which would then have to be matched by a certain orbital solution that shows a resonance transition at about the same age (e.g., Pálike et al. 2004; Ma et al. 2017). Ignoring all other physical and numerical limitations (see, e.g., Table 1), what would a more systematic search for matching solutions entail in practical terms, for now only focusing on initial conditions as a source of uncertainty?

The difference in Earth’s initial position $x_0 = (x_0, y_0, z_0)$ between DE431 and INPOP13c in each coordinate is $\sim 10^{-9}$ AU ($= d_0$, units omitted hereafter). Values within the interval, say $x_0 + d_0$, may hence be selected as new x'_0 , each of which will lead to a different numerical, orbital solution (ensemble of K total solutions). Numerically, K may then be estimated as follows (other mathematical and physical considerations aside). At double precision, as used here, the machine epsilon (ϵ) is of order 10^{-16} . Thus, if x_0 is of order 1, a set of ensemble initial conditions for x'_0 may be selected as $x'_0 = x_0 + n \cdot \epsilon$, where $n = 1, \dots, K$. Hence $K = d_0/\epsilon = 10^7$, which, combined with sets of y'_0 and z'_0 , would give 10^{21} possible initial values just for Earth’s position that could be used to generate an ensemble of numerical test solutions. In addition, similar estimates can be made for velocities and for all other bodies of the Solar System, which would give a very large number of potential initial conditions — clearly too large for practical analysis.

Just to illustrate a first step of such an approach, consider changing only Earth’s x_0 by 1×10^{-16} , for instance, in the ZB17d setup (which uses DE431). This gives a so-

lution with divergence time $\tau \simeq 57$ Myr that bears no resemblance to ZB17d, for example, around 80 Myr, except for the ubiquitous 405-kyr cycle ($g_2 - g_5$), which is omnipresent in all solutions (Fig. 11). Adding another solution with $d_0 = 1 \times 10^{-12}$ and ZB17e (based on INPOP13c), graphically illustrates several major difficulties when attempting to identify solutions with certain properties in a system with chaotic behavior (Fig. 11). First, and unsurprisingly, for times sufficiently beyond τ , the solutions do not show any systematic pattern or behavior as a function of the size of d_0 . That is, the properties of the solutions at that point appear random, regardless of whether $d_0 = 1 \times 10^{-16}$, or 1×10^{-12} , etc. Second, divergence times appear similarly arbitrary. For example, for $d_0 = 1 \times 10^{-16}$ and 1×10^{-12} , $\tau \simeq 57$ Myr and ~ 63 Myr, respectively. In other words, the solution with the larger offset in initial conditions shows ‘better’ (extended) agreement with ZB17d in the long run.

The behavior described above is characteristic for chaotic systems and merely highlights the obstacles in tracking solutions with different properties and different initial conditions (cf. eigenmode analysis, Section 4). As a result, even if it is possible to identify, say, resonance transitions in geological sequences, it is not obvious at this point how this information can be used to pinpoint a unique numerical orbital solution. Given the vast number of possible initial conditions, it is likely that a large number of solutions can be generated that will match the geological observations within data uncertainty. Conversely, can solutions at least be singled out and excluded that do not match the observations? For such an effort to be successful, generation of long, highly-quality, continuous geologic records that unequivocally identify resonance transitions should be a high priority.

6. CONCLUSIONS

The results of the present integrations lead to several conclusions regarding the factors that currently limit

the identification of a unique orbital solution beyond ~ 50 Myr. In the following, the factor with the smallest divergence time τ is considered to be currently limiting, those factors with larger τ 's are not (Table 3). If we prefer the 1un over the ems option, then the choice of the numerical algorithm at the precision tested here is not limiting; the Bulirsch-Stoer and symplectic run with 1un option agree to ~ 63 Myr. Note also that τ is not dominated by integration errors (Fig. 1), hence using, e.g., extended or quadruple instead of double precision is unlikely to affect divergence times (cf. Laskar et al. 2011a). Moreover, the step size of symplectic integrations (1un option) appears much less critical than one may think and might be increased to up to ~ 12 days for some applications (see Fig. 2). Integrations over 100 Myr could then be run in a few hours, rather than months. The potential perturbation of a hypothetical Planet 9 on Earth's orbit as tested here is not a limiting factor ($\tau \simeq 65$ Myr). Currently, the limiting factors ($\tau \simeq 54$ Myr) appear to be the number of asteroids included and uncertainties in initial conditions for positions and velocities of Solar System bodies as given by NASA and IMCCE. Overcoming these limitations should therefore be the focus of future research in order to push the limits of an astronomically-tuned geologic time scale further back in time. However, given the fundamental barriers discussed in the previous section, the path toward achieving this goal is not obvious.

Acknowledgments. I thank the anonymous reviewer for comments, which improved the manuscript. I am grateful to Bruce Runnegar and Michael Ghil for providing the numerical output of the simulations from Varadi et al. (2003), also available at: www2.hawaii.edu/~zeebe/Astro.html.

Software: HNBODY (Rauch & Hamilton 2002), SPICE (naif.jpl.nasa.gov/naif/toolkit.html), calceph (www.imcce.fr/inpop/calceph), Matlab.

REFERENCES

- Applegate, J. H., Douglas, M. R., Gursel, Y., Sussman, G. J., & Wisdom, J. 1986, *Astron. J.*, 92, 176
- Bailey, E., Batygin, K., & Brown, M. E. 2016, *Astron. J.*, 152, 126
- Batygin, K., & Brown, M. E. 2016, *Astron. J.*, 151, 22
- Batygin, K., & Laughlin, G. 2008, *Astrophys. J.*, 683, 1207
- Beck, J. G., & Giles, P. 2005, *Astrophys. J.*, 621, L153
- Brown, M. E., & Batygin, K. 2016, *Astrophys. J. Lett.*, 824, L23
- Carrington, R. C. 1863, Observations of the spots on the sun: from November 9, 1853, to March 24, 1861, made at Redhill (London: Williams & Norgate)
- Einstein, A. 1916, *Annalen der Physik*, VI. Folge, 49(7), 769
- Fienga, A., Laskar, J., Exertier, P., Manche, H., & Gastineau, M. 2015, *Celest. Mech. Dyn. Astron.*, 123, 325
- Fienga, A., Laskar, J., Kuchynka, P., et al. 2011, *Celest. Mech. Dyn. Astron.*, 111, 363
- Fienga, A., Laskar, J., Manche, H., & Gastineau, M. 2016, *Astron. Astrophys.*, 587, L8
- Fienga, A., Manche, H., Laskar, J., Gastineau, M., & Verma, A. 2014, arXiv:1405.0484
- Folkner, W. M., Williams, J. G., Boggs, D. H., Park, R. S., & Kuchynka, P. 2014, *Interplanetary Network Progress Report*, 196, 1
- Fränzl, M., & Harper, D. 2002, *Planet. Space Sci.*, 50, 217
- Giles, P. M. 2000, PhD thesis, Stanford Univ.
- Green, J. A. M., Huber, M., Waltham, D., Buzan, J., & Wells, M. 2017, *Earth Planet. Sci. Lett.*, 461, 46
- Holman, M. J., & Payne, M. J. 2016, *Astron. J.*, 152, 80
- Laskar, J. 1990, *Icarus*, 88, 266
- Laskar, J., Fienga, A., Gastineau, M., & Manche, H. 2011a, *Astron. Astrophys.*, 532, A89
- Laskar, J., & Gastineau, M. 2009, *Nature*, 459, 817
- Laskar, J., Gastineau, M., Delisle, J.-B., Farrés, A., & Fienga, A. 2011b, *Astron. Astrophys.*, 532, L4
- Laskar, J., Robutel, P., Joutel, F., et al. 2004, *Astron. Astrophys.*, 428, 261
- Ma, C., Meyers, S. R., & Sageman, B. B. 2017, *Nature*, 542, 468
- Malhotra, R. 2012, *EOLSS, UNESCO*, 6, 55
- Malhotra, R., Volk, K., & Wang, X. 2016, *Astrophys. J. Lett.*, 824, L22
- Mecheri, R., Abdelatif, T., Irbah, A., Provost, J., & Berthomieu, G. 2004, *Sol. Phys.*, 222, 191
- Millholland, S., & Laughlin, G. 2017, *AJ*, 153, 91
- Morbidelli, A. 2002, *Modern Celestial Mechanics: Aspects of Solar System Dynamics* (Taylor & Francis, London)
- Nobili, A. M., Milani, A., & Carpino, M. 1989, *Astron. Astrophys.*, 210, 313
- Pálke, H., Laskar, J., & Shackleton, N. J. 2004, *Geology*, 32, 929
- Park, R. S., Folkner, W. M., Konopliv, A. S., et al. 2017, *Astron. J.*, 153, 121
- Pijpers, F. P. 1998, *Mon. Not. R. Astron. Soc.*, 297, L76
- Pitjeva, E. V., & Pitjev, N. P. 2014, *Celest. Mech. Dyn. Astron.*, 119, 237
- Quinn, T. R., Tremaine, S., & Duncan, M. 1991, *Astron. J.*, 101, 2287
- Rauch, K. P., & Hamilton, D. P. 2002, in *Bull. Am. Astron. Soc.*, Vol. 34, AAS/Division of Dynamical Astronomy Meeting #33, 938
- Shankman, C., Kavelaars, J. J., Lawler, S. M., Gladman, B. J., & Bannister, M. T. 2017, *Astron. J.*, 153, 63
- Souami, D., & Souchay, J. 2012, *Astron. Astrophys.*, 543, A133
- Standish, E. M. 1998, *Jet Propulsion Laboratory Interoffice Memorandum*, IOM 312.F-98-048, 1
- Trujillo, C. A., & Sheppard, S. S. 2014, *Nature*, 507, 471
- Varadi, F., Runnegar, B., & Ghil, M. 2003, *Astrophys. J.*, 592, 620
- Westerhold, T., Röhl, U., & Laskar, J. 2012, *Geochem. Geophys. Geosys.*, 13, Q06015
- Wisdom, J., & Holman, M. 1991, *Astron. J.*, 102, 1528
- Zachos, J. C., Dickens, G. R., & Zeebe, R. E. 2008, *Nature*, 451, 279
- Zeebe, R. E. 2015a, *Astrophys. J.*, 798, 8
- Zeebe, R. E. 2015b, *Astrophys. J.*, 811, 9
- Zeebe, R. E., Westerhold, T., Littler, K., & Zachos, J. C. 2017, *Paleoceanogr.*, 32, 1